The effect of the deposition temperature on the low-field magnetoresistance of polycrystalline $La_{0.5}Sr_{0.5}MnO_3$ thin films produced by pulsed laser deposition



2001 J. Phys.: Condens. Matter 13 11

(http://iopscience.iop.org/0953-8984/13/1/302)

INSTITUTE OF PHYSICS PUBLISHING JOURNAL OF PHYSICS: CONDENSED MATTER

J. Phys.: Condens. Matter **13** (2001) 11–23 www.iop.org/Journals/cm PII: S0953-8984(01)15460-3

# The effect of the deposition temperature on the low-field magnetoresistance of polycrystalline $La_{0.5}Sr_{0.5}MnO_3$ thin films produced by pulsed laser deposition

**J-M Liu[1], G L Yuan[1], Q Huang[2], J Li[2], C K Ong[2], Z G Liu[1] and Y W Du[1]**

[1] Laboratory of Solid State Microstructures, Nanjing University, Nanjing 210093, China
[2] Department of Physics, National University of Singapore, 119260 Singapore

E-mail: liujm@nju.edu.cn (J-M Liu)

Received 10 July 2000, in final form 27 September 2000

**Abstract**

Pulsed laser deposition of $La_{0.5}Sr_{0.5}MnO_3$ (LSMO) thin films on quartz wafers at different deposition temperatures has been carried out. The microstructural, electrical and low-field magnetotransport properties of these films are evaluated as functions of the deposition temperature. The film crystallinity depends substantially on the deposition temperature. Significantly enhanced low-field magnetoresistance for the samples deposited from 570 °C to 600 °C, in which amorphous phase and polycrystalline phase coexist, is observed. The electrical and low-field magnetotransport properties of the thin films are explained by the two-channel model where insulating channels of variable-range-hopping conduction and metallic ones coexist.

## 1. Introduction

The manganese perovskite oxides $La_{1-x}A_xMnO_{3-y}$ (A = a divalent cation such as Ca, Sr, Ba) have been attracting special attention because they exhibit colossal magnetoresistance (CMR) [1, 2]. Although an MR ratio ($MR = [\rho(0) - \rho(H)]/\rho(0)$, where $\rho$ is the sample resistivity and $H$ is the applied magnetic field) as high as 90% has been recorded for thin-film samples in high magnetic field ($H \simeq 10^5$ Oe), the low-field MR ratio remains small. Typically, an MR ratio less than 10% was reported for epitaxial or polycrystalline $La_{1-x}Ca_xMnO_3$ (LCMO) and $La_{1-x}Sr_xMnO_3$ (LSMO) thin films at a magnetic field of a few kOe [2]. Special attention has thus been paid to the microstructure [3–12], and promising results have been reported for LCMO or LSMO samples where microscopic defects or spin-disordered media are introduced. At low temperature, they exhibit a high low-field MR ratio [4]. Introduction of spin-disordered media in the microstructures enhances the low-field MR; this is achieved by grain-size refinement and grain boundary generation [4–8], porous microstructure fabrication [9] and surface crack processing [10], in addition to lanthanide or alkaline-earth doping [13, 14]

0953-8984/01/010011+13$30.00  

and boundary deoxidization [15]. Recent work shows an enhanced low-field MR effect in two-phase perovskite oxides [16].

The MR effect is explained by the double-exchange model [17] where the ferromagnetic transition and insulating–metal transition occur almost concurrently at $T_c$ and $T_m$ respectively [2]. However, the enhanced MR ratio for the polycrystalline samples is attributed to the existence of interfaces, grain boundaries or insulating second phases [16]. At these defects the ferromagnetic spin alignment shows disordered or charge ordering, or antiferromagnetic ordering [4, 16]. The underlying physical mechanisms are the spin-polarized tunnelling (SPT) [5, 13] or spin-dependent scattering (SDS) [3] across the interfaces or boundaries. MR $\propto (M/M_s)^2$ is predicted before the magnetic saturation is reached, where $M$ is the magnetization and $M_s$ is the saturated value. As $H$ exceeds the saturation field, the MR response becomes linear.

In this article, we investigate the effect of deposition temperature on microstructural and magnetotransport properties of LSMO thin films. A simple and direct argument is given that incompletely crystallized LSMO as the second phase surrounding the crystalline LSMO may not be worse than phases such as $ZrO_2$ and $SrTiO_3$ [11, 12]. Furthermore, it is technologically beneficial to fabricate LSMO thin films at low temperature. In our work, LSMO ($x = 0.5$) is chosen for study. It is not far from the ferromagnetic/charge-ordering (CO) boundary [18]. The predicted CO transition occurs near temperature $T \sim 0$ K [19]. However, the oxygen-deficient samples may exhibit much higher CO transition temperatures—for example, oxygen-deficient LSMO ($x = 0.3$) [20]. Introduction of a small amount of the charge-ordering phase at low $T$ may enhance the MR [16], although no CO region in our samples is observed at temperature $T > 270$ K. The remaining part of this paper is organized as follows. In section 2 we give a brief description of the experimental method. The main results are reported in section 3 together with an explanation in terms of the two-channel model. The conclusions are given in section 4.

## 2. Experimental details

The LSMO ($x = 0.5$) thin films were deposited using pulsed laser deposition (PLD) on quartz wafers to avoid any effect of wafer orientation. A dense ceramic LSMO disc sintered by a standard procedure was chosen as the target. The PLD experiment was performed utilizing a KrF excimer laser of wavelength 248 nm and pulse width 30 ns. Details of the PLD procedure were reported earlier [21]. An optimized laser fluence of 1.2 J cm$^{-2}$ and frequency of 5 Hz were used during the ablation. The oxygen ambient pressure during the deposition and subsequent sequence remained constant at 0.25 mbar. The films, of 800 nm thickness and $10 \times 1.5$ mm$^2$ in-plane dimension, were deposited and then cooled down to room temperature at the same ambient pressure. No post-annealing was performed. The film thickness was measured by atomic force microscopy (AFM) and then confirmed with cross-section profiling. An *in situ* masking was used to pattern the strip-like films.

The crystallization status and grain size of the films were controlled by varying the deposition temperature $T_s$, over the range from 400 °C to 710 °C, and then checked by x-ray diffraction (XRD) and AFM. The high-resolution step-mode XRD checking was performed at the same operation condition for all samples, so a comparison of the intensity data makes sense. The microstructures of the thin films were investigated by plan-view high-resolution transmission electron microscopy (TEM). The TEM specimens were prepared by the standard preparation method. To avoid destruction of the thin-film surface, all plan-view specimens were thinned from the substrate side. The TEM observation was performed at 300 kV on a Philips CM 300.

An Oxford superconducting vibrating-sample magnetometer (VSM) was used to characterize the magnetization $M$ and magnetic hysteresis of the samples [21]. The electrotransport and magnetotransport properties were measured by the standard four-pad probing method with data collected by a PC machine. The triangle-wave AC magnetic field, $\pm 4$ kOe in magnitude and 0.01 Hz in frequency, was applied parallel to the sample surface. A field of $\sim$4 kOe is viewed as the low field here. The sample temperature can be stabilized within an uncertainty of $\pm 0.2$ K.

## 3. Results and discussion

### *3.1. Microstructure*

Figure 1 presents the XRD spectra for a series of samples deposited at different $T_s$. The diffraction spectrum for the target is included too. The samples deposited at $T_s < 530$ °C show no identifiable reflection, and thus are completely amorphous. At $T_s = 530$ °C, just weak (110) reflection is recorded. The FWHM (full width at half-maximum) is $\sim$0.65 °, three times that of the target. At $T_s = 550$ °C, 570 °C and 600 °C there appear (111), (200) and (211) reflections besides the preferential (110). These peaks are quite weak in comparison with

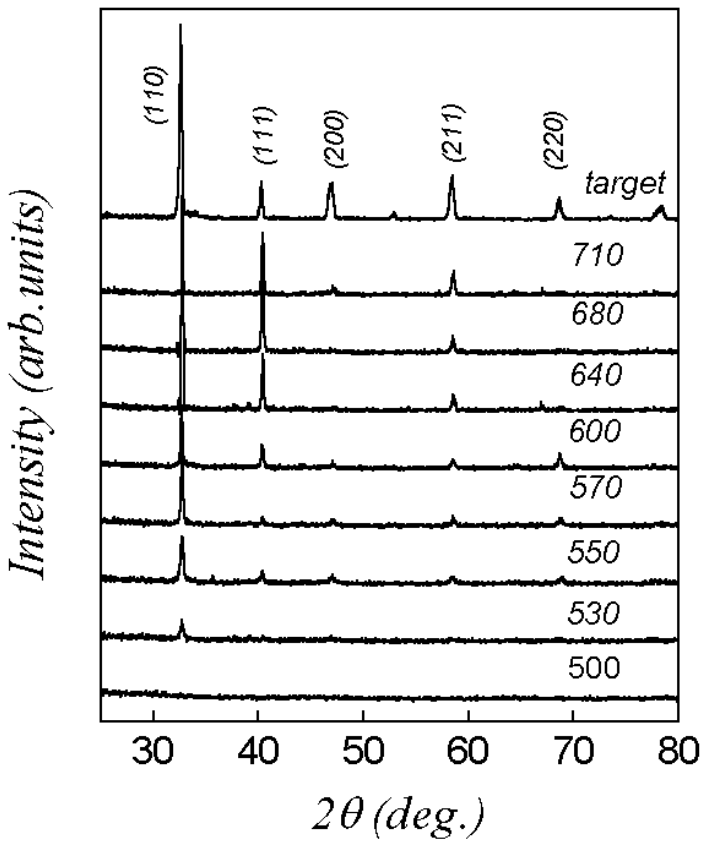


**Figure 1.** XRD $\theta$–$2\theta$ spectra for a series of LSMO thin films deposited at different values of $T_s$ as indicated numerically. The spectrum of the ceramic LSMO target is inserted too.

those from the target and the films deposited at higher $T_s$. We may argue that these samples contain a lot of incomplete crystalline and amorphous phases. For convenience, we call them amorphous, noting that they may not be strictly amorphous in the crystallographic sense.

The TEM observation confirms the above argument. Figures 2(a) and 2(b) present the TEM images of the sample deposited at $T_s = 600\,^{\circ}$C. The white and pale regions in figure 2(a) image respectively the amorphous and crystalline phases, confirmed with corresponding electron diffraction patterns. The inter-crystal separation is $\sim$10 nm or more. The high-resolution imaging clearly produces fringes of the crystalline grains, as shown in figure 2(b). The fringe

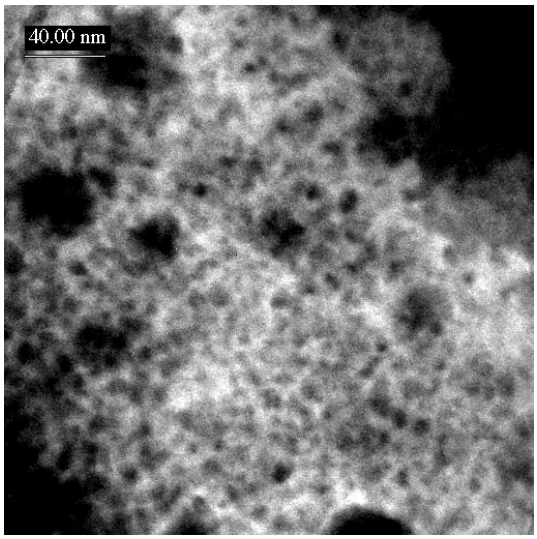


(a)

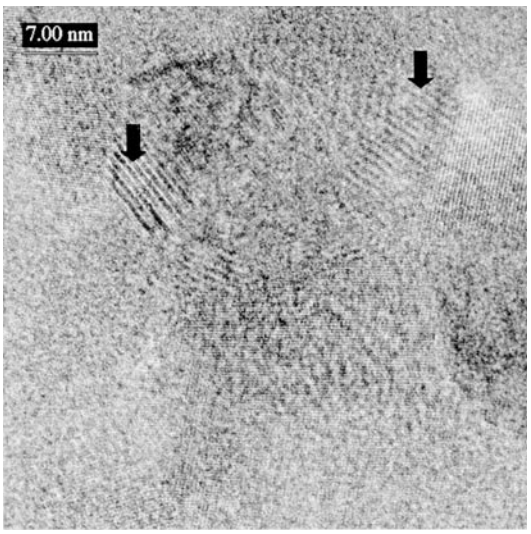


(b)

**Figure 2.** TEM images of LSMO thin film deposited at 600 °C. The arrows indicate superlattice regions with spacing of double the lattice constant.

spacing is ∼0.4 nm, consistent with the lattice constant of LSMO. The grey regions between two crystals represent the amorphous layers. For this sample, a relative volume proportion of ∼40% for the crystalline phase is estimated. The two-phase microstructure shown in figure 2 is quite similar to the two-phase percolation pattern as reported by Uehara *et al* [16], but here the insulating phase is amorphous LSMO instead of CO phase. The two phases probably form separated chain-like patterns over the sample, although the number of amorphous or crystal chains may depend substantially on $T_s$. For example, at lower $T_s$ the crystalline chains may be less frequently observable or even disappear at $T_s < 530$ °C. In contrast, the sample deposited at $T_s > 700$ °C may no longer contain any amorphous chains.

Our TEM observation does not show any CO region at $T > 270$ K, although the possibility of the appearance of CO at low $T$ (say, 77 K) cannot be excluded. The coarse strips as indicated by black arrows in figure 2(b) have an inter-strip spacing of ∼0.8 nm, double the lattice spacing but much smaller than the CO strip spacing for LSMO. Furthermore, an abnormal change of the electrotransport and magnetotransport properties of the samples (resistivity $\rho$ and magnetization $M$) at some $T$ would be observed if CO regions appeared. However, such an abnormal change does not occur.

At $T_s = 680$ °C, the thin film shows a spectrum quite similar to that of the target. The sample consists of a complete polycrystalline phase. The AFM observation shows that the grain size, if observable, does not change much as $T_s$ differs. The average grain size for samples deposited between 550 °C and 600 °C is 50–80 nm, but no clear grain boundary layer can be distinguished within the best resolution of AFM. This value is larger than that evaluated from TEM. At $T_s = 640$ °C and over, the grains of 70–100 nm average size and grain boundaries (GBs) are clearly observable.

These results indicate a considerable effect of $T_s$ on the film microstructure. With the TEM evidence, we argue that the microstructure for the samples deposited at $T_s = 600$ °C and lower consists of crystalline LSMO grains and amorphous LSMO phase, or even a single amorphous phase at lower $T_s$. The latter, however, disappears when the deposition is performed at 680 °C and over. The sample just consists then of polycrystalline grains with well-defined GBs.

### *3.2. Magnetotransport*

The magnetotransport response of the deposited samples is measured. As an example, the resistivity $\rho$ at $T = 77$ K for the sample deposited at $T_s = 600$ °C is plotted in figure 3(a). The magnetic field $H$ and recorded fluctuations of $T$ are inserted for reference. The MR–$H$ hysteresis (represented here by $\rho/\rho_0$; MR $= 1 - \rho/\rho_0$) for three samples deposited at $T_s = 550$ °C, 600 °C and 680 °C, respectively, is presented in figure 3(b).

Several features associated with the hysteresis are worthy of mention. First, the MR peak location is the same as for the coercivity $H_c$, confirmed by plotting in the same figure the MR–$H$ loop and $M$–$H$ loop together, as shown in figure 7 below. Second, the MR response can be roughly classified into two parts. In part I where $|H| \leqslant 700$ Oe, the response is nonlinear and associated with the ferromagnetic domain dynamics [3, 4]. For part II where $|H| > 2$ kOe, a roughly linear decrease of $\rho$ with increasing $|H|$ is obtained, which is primarily attributed to the amorphous phase. Finally, the MR response in part II shows substantial scatter as $T_s$ differs, whereas for part I the three curves overlap. This result predicts a significant influence of the amorphous phase.

The zero-field resistivity $\rho_0$ and MR ratio at $H = 4$ kOe as functions of $T$ for the samples are presented in figure 4. All samples show insulator-like transport behaviour. At $T_s < 530$ °C, the resistivity is too high to be measurable. As $T_s$ increases from 530 °C to 600 °C, $\rho_0(T = 77\ \text{K})$ shows a rapid decrease from 200 Ω cm to just 0.4 Ω cm, down

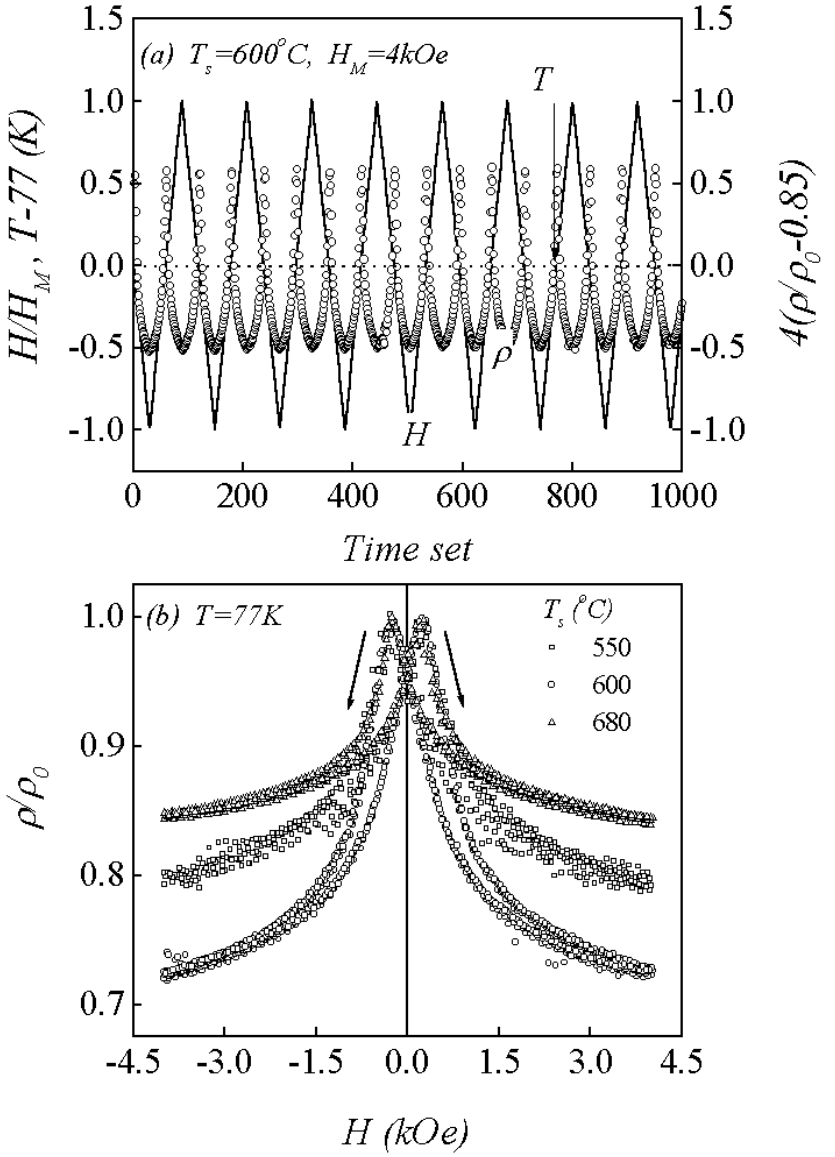


**Figure 3.** (a) Magnetic field $H$ (solid line), recorded MR ratio ($\rho/\rho_0$) (open circles) and temperature $T$ (dotted line) as functions of time for the LSMO film deposited at 600 °C. (b) $\rho/\rho_0$–$H$ hysteresis loops at $T = 77$ K for three LSMO films deposited at 550 °C, 600 °C and 680 °C.

three orders of magnitude. The resistivity does not decrease much when $T_s$ increases further. $\rho_0$(77 K) remains around a few Ω mm. On the other hand, the sample prepared at $T_s = 530$ °C shows a linear log $\rho_0$–$T$ dependence. For the samples deposited at higher $T_s$, the low-$T$ part of the log $\rho_0$–$T$ relation begins to deviate negatively from the linear dependence.

The low-temperature MR ratio depends substantially on $T_s$. Taking the data at $T = 77$ K, we see a growth of the MR ratio from 16% for $T_s = 530$ °C to 29% for $T_s = 600$ °C, and then a decay back by just 13% for $T_s = 710$ °C. Combining this with our understanding of the microstructure, it has become clearly evident that the single-phased polycrystalline films

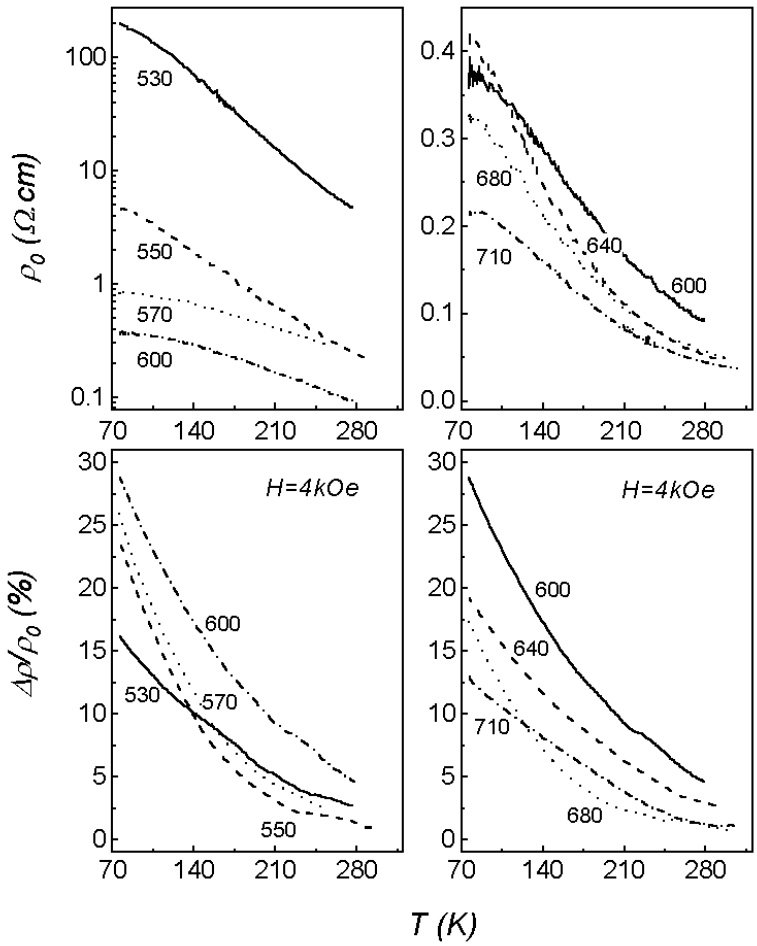


**Figure 4.** Zero-field resistivity $\rho_0$ (top row) and MR ratio $\Delta\rho/\rho_0$ at $H = 4$ kOe (bottom row) as functions of temperature for a series of samples deposited at different values of $T_s$ as indicated.

show much lower MR than the multi-phase films. Keeping in mind our analysis of figure 3(b), it can be concluded that mixing of the amorphous phase with the polycrystalline phase, here with the help of low-temperature deposition, is a useful way to enhance the low-field MR in LSMO thin films. The amount and distribution of the amorphous phase as controlled by the deposition temperature are easily optimized in terms of the MR ratio. In our experiment, the optimized value of $T_s$ covers from 570 °C to 600 °C.

### *3.3. The two-channel mechanism*

The as-induced MR enhancement can be explained by a modified scheme based on the two-channel model developed by de Andres *et al* [6]. In this modified model, two types of conduction channel aligned in parallel in the microstructure are supposed. One is the metallic conduction channel (MCC) and the other is the insulator conduction one (ICC). By means of this model, the sample can be divided into the two types of channel set, as shown schematically in figure 5. Here the MCC covers the crystalline grains that are supposed to contact intimately

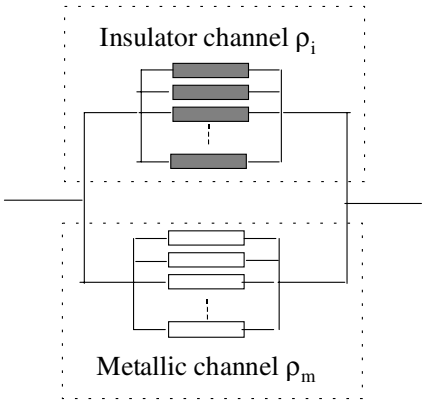


**Figure 5.** A schematic drawing of the two-channel conduction picture.

through GBs if they are neighbouring, although some GBs themselves represent defective states. The ICC is composed of the amorphous phase chains. These chains are supposed to align in parallel in our system. They are not necessarily straight and may interact with one and another. Of course, one can also map the microstructure onto a network of the insulating and metallic phases, so the two-phase alignments can be partly in series. However, such a scheme is not convenient for deriving $\rho_0$ and MR as functions of the microstructure, as is to be done in the next subsection.

For the scheme as shown in figure 5, the resistivities for the ICC and MCC are represented by $\rho_i$ and $\rho_m$, respectively. All MCCs and ICCs are supposed identical, respectively. Therefore, the total resistivity $\rho$ for the sample is expressed as

$$\rho = \left(\frac{1}{\rho_i} + g\frac{1}{\rho_m}\right)^{-1} \tag{1}$$

where $g$ is a geometric parameter that characterizes the proportion of MCCs relative to ICCs. $\rho_i$ for the ICC (amorphous here) can be formulated in terms of the variable-range-hopping (VRH) model [2, 6], yielding

$$\rho_i = \rho_{i0}\exp(T_0/T)^{1/4} \tag{2a}$$

where $\rho_{i0}$ is the pre-factor and $T_0$ is the characteristic temperature for VRH.

On the other hand, $\rho_m$ for LSMO as a function of $T$ at low $T$ can be fitted as [22]

$$\rho_m = \rho_{m0} + \rho_{m1}T + \rho_{m2}T^2 + \rho_{m4}T^{4.5} \tag{2b}$$

where $\rho_{mi}$ ($i = 0$, 1, 2 and 4) are positive constants. However, so many parameters to be determined makes a successful fitting of the data with equation (1) impossible. Taking into account that the higher-order contribution is small, as the first-order approximation, $\rho_m$ for the MCC is simplified to

$$\rho_m = a + bT \tag{2c}$$

where $a$ and $b$ are two constants. Our pre-calculation did indeed show $\rho_{m4}T^{4.5}$ and $\rho_{m2}T^2$ to be much smaller than $\rho_{m1}T$. Therefore, $\rho$ can be rewritten as

$$\rho = \left\{\frac{1}{\rho_{i0}\exp(T_0/T)^{1/4}} + \frac{g/a}{1+(b/a)T}\right\}^{-1}. \tag{3}$$

The four parameters, $\rho_{i0}$, $T_0$, $g/a$ and $b/a$, are evaluated by best fitting with equation (3) the resistivity data as presented in figure 4. It is revealed that the parameter $b/a$ is nearly

**Table 1.** Four parameters, $\rho_{i0}$, $T_0$, $g/a$ and $b/a$, as derived from the resistivity fittings with equation (1) under zero field and $H = 4$ kOe. $R$ is the fitting reliability factor.

| $T_s$ (°C) | $H$ (kOe) | $\rho_{i0}$ (Ω cm) | $R$ | $T_0$ (K) | $R$ |
|---|---|---|---|---|---|
| 530 | 0 | $2.30142 \times 10^{-6}$ | >0.91 | $1.33887 \times 10^{7}$ | >0.87 |
| | 4 | $2.90324 \times 10^{-6}$ | >0.92 | $1.23833 \times 10^{7}$ | >0.88 |
| 550 | 0 | $1.9603 \times 10^{-6}$ | >0.94 | $6.45319 \times 10^{6}$ | >0.90 |
| | 4 | $2.06124 \times 10^{-6}$ | >0.94 | $4.90637 \times 10^{6}$ | >0.89 |
| 570 | 0 | $2.94039 \times 10^{-6}$ | >0.98 | $3.00854 \times 10^{6}$ | >0.94 |
| | 4 | $1.64826 \times 10^{-6}$ | >0.98 | $9.9454 \times 10^{6}$ | >0.93 |
| 600 | 0 | $1.62593 \times 10^{-6}$ | >0.99 | $4.69226 \times 10^{6}$ | >0.98 |
| | 4 | $8.78905 \times 10^{-7}$ | >0.99 | $6.27783 \times 10^{6}$ | >0.98 |
| 640 | 0 | $1.09253 \times 10^{-6}$ | >0.99 | $5.19456 \times 10^{6}$ | >0.98 |
| | 4 | $8.4117 \times 10^{-7}$ | >0.99 | $4.37357 \times 10^{6}$ | >0.98 |
| 680 | 0 | $9.90776 \times 10^{-7}$ | >0.97 | $4.22761 \times 10^{6}$ | >0.91 |
| | 4 | $7.06396 \times 10^{-7}$ | >0.95 | $5.38337 \times 10^{6}$ | >0.90 |
| 710 | 0 | $6.89526 \times 10^{-7}$ | >0.92 | $5.44451 \times 10^{6}$ | >0.87 |
| | 4 | $5.78997 \times 10^{-7}$ | >0.90 | $4.13625 \times 10^{6}$ | >0.90 |
| $T_s$ (°C) | $H$ (kOe) | $g/a$ ($\Omega^{-1}$ cm$^{-1}$) | $R$ | $b/a$ ($K^{-1}$) | $R$ |
| 530 | 0 | 0.00477 | >0.82 | $8.4 \times 10^{-4}$ | >0.85 |
| | 4 | 0.00553 | >0.80 | | |
| 550 | 0 | 0.1926 | >0.87 | | |
| | 4 | 0.24588 | >0.87 | | |
| 570 | 0 | 1.18612 | >0.84 | | |
| | 4 | 1.6908 | >0.84 | | |
| 600 | 0 | 2.73096 | >0.90 | | |
| | 4 | 3.81144 | >0.90 | | |
| 640 | 0 | 2.3619 | >0.93 | | |
| | 4 | 2.78409 | >0.95 | | |
| 680 | 0 | 3.03284 | >0.92 | | |
| | 4 | 3.74948 | >0.94 | | |
| 710 | 0 | 4.67682 | >0.90 | | |
| | 4 | 4.9688 | >0.91 | | |

$T_s$-independent, which leads to the prediction that the transport properties of the crystalline LSMO grains change little once they form at a certain deposition temperature. We then fix $b/a = 8.4 \times 10^{-4}$ $K^{-1}$ and evaluate the other parameters in order to improve the fitting reliability. The fitted data for zero field and $H = 4$ kOe as a function of $T_s$ are listed in table 1 together with the fitting reliability and also plotted in figures 6(a)–6(c). For the ICC, it is clearly established that $\rho_{i0}$ at both zero field and $H = 4$ kOe drops rapidly with increasing $T_s$ for the low-$T_s$ range. As $T_s$ exceeds 640 °C, the dropping is substantially slowed down. The change of the characteristic temperature $T_0$ as a function of $T_s$ is similar. When $T_s$ increases, the ground-state conduction for the channel is significantly improved (sharply dropping $\rho_{i0}$). Note that $\rho_{i0}$ tends to become saturated as $T_s$ exceeds 640 °C.

On the other hand, for a fixed $T_s$, the difference either between $\rho_{i0}(H = 0)$ and $\rho_{i0}(H = 4$ kOe) (note that $\rho_{i0}(0) > \rho_{i0}(4$ kOe)) or between $T_0(0)$ and $T_0(4$ kOe) (note that $T_0(0) < T_0(4$ kOe)) is really not remarkable in spite of being identifiable. The biggest relative difference for either $\rho_{i0}$ or $T_0$ appears at $T_s = 570$ °C and 600 °C. The carrier

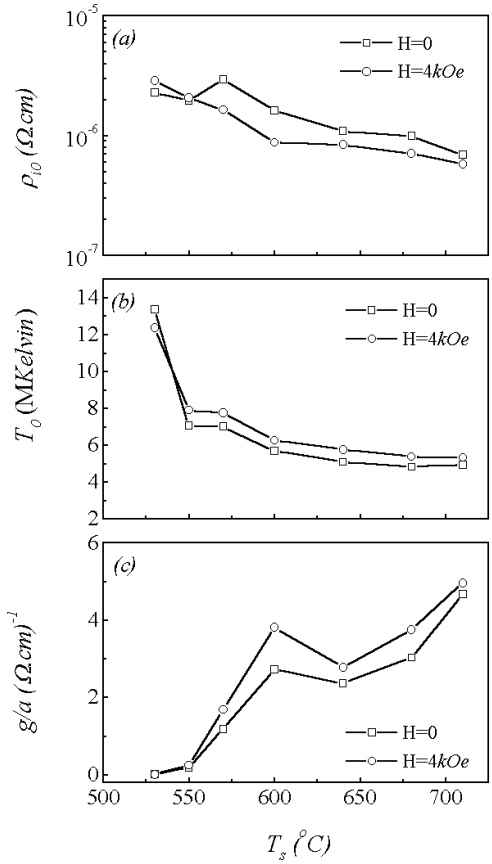


**Figure 6.** (a) Pre-factor $\rho_{i0}$, (b) characteristic temperature $T_0$ and (c) geometrical parameter $g/a$ as functions of $T_s$, at $H = 0$ (squares) and 4 kOe (circles) for the LSMO thin films.

density at the Fermi surface, $N(E_F)$, can be estimated according to the VRH model. Taking $T_0 = 7 \times 10^6$ K and the localization length $\xi \sim 0.4$ nm (the Mn–Mn separation in LSMO), $N(E_F) \sim 2.30 \times 10^{26}$ eV$^{-1}$ m$^{-3}$ is yielded via [23]

$$kT_0 = \frac{24}{\pi N(E_F)\xi^3} \tag{4}$$

where $k$ is the Boltzmann constant. This value is two orders of magnitude lower than that for single-crystal LSMO [24]. An embedding of the amorphous phase in the microstructure makes a fraction of the carriers localized.

The parameter $g/a$ as a function of $T_s$ is presented in figure 6(c), for $H = 0$ and 4 kOe. It starts to grow as $T_s$ exceeds 550 °C until 600 °C is reached. Afterwards the growth slows down. Because $g/a$ characterizes the relative amount of the metallic channel in the microstructure, the amount of the insulating channel decreases rapidly with increasing $T_s$ for the low-$T_s$ range but not so much for $T_s \geqslant 640$ °C. This prediction is supported by the microstructural evolution. Comparing with the tiny change of $\rho_{i0}$ and $T_0$, the change of $g/a$ induced by applying a magnetic field is very remarkable once $T_s$ exceeds 550 °C. This change characterizes the magnitude of the MR ratio, to be calculated below.

### *3.4. Magnetoresistance enhancement*

For convenience, we rewrite equation (1) as

$$\sigma = \sigma_i + g\sigma_m \tag{5}$$

where $\sigma$ represents the total electrical conductivity, and $\sigma_i$ and $\sigma_m$ those for the ICC and the MCC, respectively. Since $\sigma_i$ has been proven to change little against magnetic field and $\sigma_i \ll g\sigma_m$, the MR ratio can be roughly written as

$$\mathrm{MR} = \frac{\sigma(H) - \sigma(0)}{\sigma(H)} \approx \frac{\sigma_m(H) - \sigma_m(0)}{\sigma_m(H)} + \frac{g(H) - g(0)}{g(H)} \frac{\sigma_m(0)}{\sigma_m(H)} \approx \frac{\Delta\sigma_m}{\sigma_m(H)} + \frac{\Delta(g/a)}{(g/a)(H)} \tag{6}$$

where $\sigma_m(0) \sim \sigma_m(H)$ is assumed to simplify the second term on the right-hand side, noting that $\Delta\sigma$ is anyway much smaller than $\sigma$.

We can prove that the first term on the right-hand side of equation (6) takes account of the MR ratio at very low field ($H \sim H_c$) and the second term is mainly the contribution at high field ($H \gg H_c$). The resistivity reduction at low field (lower than the field for saturated magnetization) is attributed to movement of the domain walls and spin rotation, if any, at the walls; i.e. [3, 4],

$$\mathrm{MR} = \Delta\rho/\rho(0) = \Delta\sigma_m/\sigma_m(H) \propto (M/M_s)^2. \tag{7}$$

A comparison of equation (7) with equation (6) gives $\Delta g = 0$. As a verification of equation (7), figure 7 gives the $\Delta\rho/\rho_0$–$H$ and $M$–$H$ loops for the sample deposited at $T_s = 680\ ^\circ$C. It is easily demonstrated that equation (7) is actually satisfied as long as $H \leqslant 700$ Oe. Looking back at figure 3(b), one sees that the $\Delta\rho/\rho_0$–$H$ loops for the three deposition temperatures show quite satisfactory overlaps for very low field ($H < 700$ Oe), demonstrating the independence of $\Delta\rho/\rho_0$ of the parameter $g/a$, and thus $T_s$.

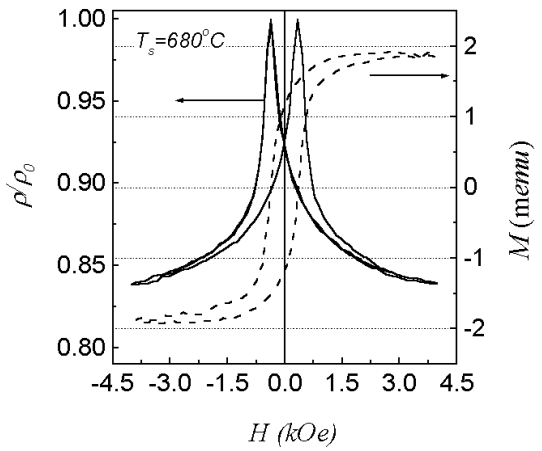


**Figure 7.** The $\rho/\rho_0$–$H$ loop and $M$–$H$ loops measured at 77 K for the LSMO thin films deposited at 680 °C.

As $H$ is much higher than that required for $M = M_s$, the MR ratio becomes dependent on $g/a$. Taking the zero-order approximation and also noting that

$$\frac{\Delta\sigma_m}{\sigma_m(H)} \ll \frac{\Delta(g/a)}{(g/a)(H)}$$

for the data for the lower-$T_s$ range, equation (6) is simplified to

$$\mathrm{MR} \approx \frac{\Delta(g/a)}{(g/a)(H)}. \tag{8}$$

Plotting the measured MR ratio and calculated MR ratio via equation (8) and figure 6(c) at $H = 4$ kOe yields very good coincidence, as shown in figure 8. The two-channel model seems a good description of the magnetotransport behaviour in our systems. The difference for the high-$T_s$ range (680 °C and 710 °C) is due to the fact that equation (8) is no longer a good approach because the term $\Delta\sigma_m/\sigma_m(H)$ in equation (6) is not negligible any more. The real MR ratio should be larger than that given by equation (8), just as shown in figure 8.

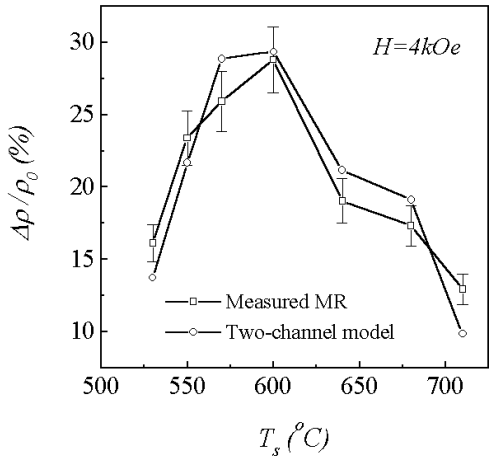


**Figure 8.** Measured MR ratio (squares with error bars) and calculated MR ratio (circles) from the two-channel model as functions of $T_s$.

## 4. Conclusions

In conclusion, we have investigated in detail the effect of the deposition temperature on the microstructural, electrical and magnetoresistance properties of LSMO thin films deposited on quartz wafers. A significant influence of the deposition temperature on these properties has been revealed. It has been confirmed that coexistence of insulating amorphous and metallic polycrystalline grains in the films is beneficial to enhancement of the low-field magnetoresistance. A substantially enhanced 77 K MR ratio of ∼30% at $H = 4$ kOe for the films deposited at 570 °C and 600 °C has been obtained. The two-channel model in which the insulator channels and metallic channels align in parallel has been used to explain the conductivity and magnetotransport behaviours for the thin films deposited at low temperature, and a quite good consistency between the measured results and predicted ones is shown.

## Acknowledgments

The authors would like to acknowledge support from the National Natural Science Foundation of China through normal and special projects, the National Key Project for Basic Research of China and LSSMS of Nanjing University.

## References


[1] Jin S, Tiefel T H, McCormack M, Fastnacht R A, Ramesh R and Chen L H 1994 *Science* **264** 413
[2] Rao C N R and Raveau B 1998 *Colossal Magnetoresistance, Charge Ordering and Related Properties of Manganese Oxides* ed C N R Rao and B Raveau (Singapore: World Scientific) p 189
[3] Li X W, Gupta A, Xiao G and Gong G Q 1997 *Appl. Phys. Lett.* **71** 1124
[4] Gupta A 1998 *Colossal Magnetoresistance, Charge Ordering and Related Properties of Manganese Oxides* ed C N R Rao and B Raveau (Singapore: World Scientific)
[5] Lee S, Hwang H Y, Shraiman B I, Ratcliff W D and Cheong S-W 1999 *Phys. Rev. Lett.* **82** 4508
[6] de Andres A, Garcia-Hernandez M, Martinez J L and Prieto C 1999 *Appl. Phys. Lett.* **74** 3884
[7] Balcells L, Fontcuberta J, Martinez B and Obradors X 1998 *Phys. Rev.* B **58** R14 679
[8] Hwang H Y, Cheong S-W, Ong N P and Batlogg B 1996 *Phys. Rev. Lett.* **77** 2041
[9] Wang X L, Dou S X, Liu H K, Ionescu M and Zeimetz B 1998 *Appl. Phys. Lett.* **73** 396
[10] Peng H B, Zhao B R, Xie Z, Lin Y, Zhu B Y, Hao Z, Ni Y M, Tao H J, Dong X L and Xu B 1999 *Appl. Phys. Lett.* **74** 1606
[11] Balcells L, Carrillo A E, Martinez B and Fontcuberta J 1999 *Appl. Phys. Lett.* **74** 4014
[12] Petrov D K, Krusin-Elbaum L, Sun J Z, Field C and Duncombe P R 1999 *Appl. Phys. Lett.* **75** 995
[13] Hwang H Y, Cheong S W, Radaelli P G, Marezio M and Batlogg B 1995 *Phys. Rev. Lett.* **75** 914
[14] Fontcuberta J, Martinez B, Seffar A, Pinol S, Garcia-Munoz J L and Obradors X 1996 *Phys. Rev. Lett.* **76** 1122
[15] Huang Q, Ong C K, Liu J-M and Li J, unpublished
[16] Uehara M, Mori S, Chen C H and Cheong S-W 1999 *Nature* **399** 560
[17] Zener C 1951 *Phys. Rev.* **82** 403
[18] Jonker G H 1956 *Physica* **22** 707
[19] Rao C N R and Raychaudhuri A K 1998 *Colossal Magnetoresistance, Charge Ordering and Related Properties of Manganese Oxides* ed C N R Rao and B Raveau (Singapore: World Scientific) p 37
[20] Li J, Ong C K, Liu J-M and Huang Q 2000 *Appl. Phys. Lett.* **76** 1051
[21] Li J, J-M Liu, Li H P, Fang H C and Ong C K 1999 *J. Magn. Magn. Mater.* **202** 285
[22] Schiffer P, Ramirez A P, Bao W and Cheong S-W 1995 *Phys. Rev. Lett.* **75** 3336
[23] Ziese M and Srinitiwarawong C 1998 *Phys. Rev.* B **58** 11 519
[24] Woodfield B F, Wilson M L and Byers J M 1997 *Phys. Rev. Lett.* **78** 3201